Indian Journal of Chemical Technology
Vol. 30, May, 2023 pp. 320-330
DOI: 10.56042/ijct.v30i3.61561

Hydrothermal synthesis of mesoporous TiO_2 nanoparticles for enhanced photocatalytic degradation of organic dye

Md. Tamez Uddin*, Joyanta Mondal, Shafiul Hossain & Muhammad Zobayer Bin Mukhlish

Department of Chemical Engineering and Polymer Science, Shahjalal University of Science and Technology, Sylhet 3100, Bangladesh

E-mail: mtuddin-cep@sust.edu

Received 18 March 2022; accepted 15 February 2023

In this work, mesoporous TiO_2 nanoparticle photocatalyst has been prepared by hydrothermal method using titanium tetrachloride as precursor. The resulting photocatalysts have been characterized using X-ray diffraction (XRD), nitrogen adsorption-desorption analyses, RAMAN spectroscopy, Transmission Electron Microscopy (TEM) and UV-vis diffuse reflectance spectroscopy (UV-vis DRS). The results showed that the synthesized OiT_2 was anatase phase and mesoporous with specific surface 133.45 m^2/g. The decomposition of methylene blue dye under the influence of ultraviolet light was used to test the photocatalytic performance of the produced TiO_2 photocatalyst. The photocatalytic activity of the TiO_2 photocatalyst for the breakdown of methylene blue dye was significantly higher than that of the commercial TiO_2 P25 used as a reference. Moreover, the prepared photocatalyst was stable and reusable. The larger surface area of hydrothermally produced TiO_2 was the reason for this enhanced photocatalytic activity. As a result, it is expected that this approach of photocatalytically active semiconducting nanocatalysts will be used in industry to eliminate undesired organics from the environment.

Keywords: Degradation, Dyes, Hydrothermal method, Photocatalyst, TO_2 nanoparticles

Synthetic dyes are significantly used in many chemical industries to color their final products [1–3]. It is projected that more than 10,000 different dyes and pigments are used in industry, with over 7×10^5 tons of synthetic dyes manufactured annually[4,5]. About two-thirds of the dyes are used in textile industry, around 10-15% of which is emerged as effluent [2]. The dyeing process in the textile industry consumes a significant amount of water. Textile plant effluents are classified as the most polluting of all industrial sectors, both in terms of volume produced and effluent composition[6-9]. Furthermore, the demand for textiles and resulting increases in production, as well as the use of synthetic dyes, have all contributed to dye wastewater being one of the most serious sources of pollution in recent years[4,10]. Textile effluent should not be released into the environment because the dye inhibits re-oxygenation of water bodies by obstructing penetration of sunlight[11,12]. It also raises BOD and causes a lack of dissolved oxygen, which is essential for marine life to survive. Furthermore, most dyes used as coloring materials are harmful to certain microorganisms and aquatic life, even at very low concentrations, and may cause inhibition of their catalytic abilities[13]. Since many dyes are immune to aerobic digestion, they are difficult to degrade. Dyes can also irritate the skin and cause allergic dermatitis. It has been discovered that some of them are carcinogenic and mutagenic[14-16]. Dye pollution is not only a major public health issue, but it also has the potential to cause serious environmental issues due to its persistence. As a result, extracting the dye content from effluents prior to disposal is important.

Over the past decades, heterogeneous photocatalysis on semiconducting oxide photocatalyst has received a lot of interest due to its efficiency in degrading organic contaminants in water and air[17–23]. In this process, exposing a semiconductor photocatalyst to light with an energy higher than the band gap of the semiconductor excites electrons from the valence band to the conduction band, resulting in the formation of charge carriers [electron-hole pair (e^- -h^+)]. The photogenerated electron-holes react with adsorbed water, surface hydroxyl (OH) groups and oxygen and create reactive species as hydroxyl radicals ($^{\bullet}OH$) and superoxide radical anion ($O_2^{\bullet-}$) which have high oxidation potential to decompose adsorbed organic compounds into CO_2

and H_2O[24–26]. To date, titanium oxide (TiO_2) is one of the most commonly employed photocatalysts in industrial wastewater treatment because of its high oxidizing power, stability, appropriate band positions, low cost, and non-toxicity to living beings[27–31]. However, the photocatalytic activity of TiO_2 is influenced by its surface and structural features like crystal structure, surface area, size distribution, porosity, and band gap energy[32]. It has been reported that the limited surface area of TiO_2 and the fast recombination of photogenerated charge carriers impede its use[24,33]. So far, a variety of methods for increasing the photocatalytic activity of TiO_2 have been described, including the doping of noble metals, heterojunction forming, morphological tuning, oxygen vacancy creation, and surface modification[34-37]. Nevertheless, doping and coupling of TiO_2 often leads in high carrier recombination rates and thermal instability as secondary impurities can function as carrier recombination sites, reducing the efficiency of TiO_2 photocatalyst. There are three crystallographic forms of TiO_2like rutile, anatase and brookite[38,39]. Rutile is the most stable of the three crystallographic forms of TiO_2, while anatase and brookite are metastable and quickly changed to rutile when heated[40-42]. According to previous research, the anatase phase has been found to be more photocatalytically active than the rutile phase due to the rapid recombination of photogenerated charge carriers in the rutile phase[43-45]. Recently brookite phase has been shown to outperform rutile and anatase in photocatalytic oxidation reactions[46,47]. It is, however, extremely difficult to produce pure brookite without rutile or anatase, so the photocatalytic activities of brookite have not been extensively studied until recently. As a result, developing pure anatase phase TiO_2 with a high surface area is required to achieve its superior photocatalytic activity.

There are a number of ways to produce nanocrystalline TiO_2, including sol–gel[48,49], chemical vapor deposition (CVD)[50-52], sputtering[53,54], solvothermal[55-57], sonochemical[58,59], solution combustion method[60-63], microemulsion[64,65], inverse micelle methods[66,67] and microwave assisted method[68,69]. The majority of synthetic procedures begin with the production of amorphous TiO_2 nanoparticles with a large surface area, which are then subjected to high temperature treatment in the second stage. Surface area is substantially reduced after high-temperature treatment when amorphous TiO_2 transforms into crystallized TiO_2. As a result, traditional preparation methods that include the calcination of amorphous titanium seldom result in significant surface areas, which is a key factor in heterogeneous photocatalysis. Recently, the hydrothermal method has received a lot of attention as an effective approach for synthesizing nanoparticles with high surface area, extremely crystalline, high-purity and homogeneity. The hydrothermal approach has previously been used to develop titania polymorphs with various morphologies from various precursors[70-73]. The starting precursors have a substantial effect on the formation of anatase TiO_2 nanocrystallites with a well-defined crystalline morphology. It is reported that the hydrothermal treatment of amorphous TiO_2 used as starting material in the presence of different acids such as HF, HCl, HNO_3, and citric acids led to the formation of a mixture of anatase, brookite and rutile nanocrystallites[73]. In another study, nanosized anatase titanium dioxide was synthesized by hydrothermal crystallization of amorphous titanium dioxide employing hydrogen fluoride and hydrogen chloride as cooperative catalysts[72].In the present study, pure anatase TiO_2 has been synthesized by hydrothermal treatment of TiO_2 suspension in presence of acetic acid where TiO_2 suspension was synthesized by hydrolysis of $TiCl_4$ with ammonia solution. The effect of hydrothermal temperature on crystallinity and surface area has been studied. The prepared TiO_2 has been characterized with different techniques. The photocatalytic activity of the synthesized photocatalyst has been determined by decomposing methylene blue dye under UV light irradiation. Experiments with commercially available photocatalysts, Degussa P25, were also carried out for comparison.

Experimental Section

Synthesis of TiO_2 NPs

All chemical reagents were purchased from Merck, Germany and Merck, India and were used just as they were obtained, with no more purifying. TiO_2 was prepared by hydrothermal method using titanium tetrachloride ($TiCl_4$) as precursor. A typical approach involved dissolving 2 mL $TiCl_4$ in 25 mL deionized water and stirring the resultant solution for 1 hour at room temperature. Following that, aqueous solution of ammonium hydroxide (NH_4OH) was added dropwise to achieve a *p*H value of 7 while vigorous stirring was carried out throughout. The stirring was continued for 4 h and the resulting precipitate was

then centrifuged and washed with distilled water for several time to get chloride free precipitate. The precipitate was then dispersed in 25 mL water acidified with acetic acid and was subjected to hydrothermal treatment at different temperatures (120, 150, 200, 220°C) for 16 h. After cooling to room temperature, the TiO_2 was centrifuged, rinsed several times with water, and dried at 110°C overnight.

The X-ray diffraction (XRD) measurement was carried out with Rigaku Smart Lab X-ray diffractometer (Rigaku, SmartLab, Japan) in order to confirm the formation of TiO_2, crystalline phase as well as size of crystallite. In order to obtain the 2θ data, the sample was scanned in the 2θ range of 10 to 80°. Scherrer's formula was used to determine the mean size of crystallites in the sample. The morphology and the size of TiO_2 NCs were studied using Transmission Electron Microscopy (TEM) (Talos F200X, Thermofisher scientific, USA) with an accelerating voltage of 200 kV. In order to prepare the sample, the photocatalysts were dispersed in ethanol using an ultrasonic bath (high purity ethanol 99.8% and a tiny droplet of the suspension was deposited on a Cu plate. UV-vis-NIR spectrometer (LAMDA 750, Perkin-Elmer, Inc, USA) was used to determine the energy band gap of the prepared NPs under normal circumstances. The UV-vis DRS was measured by scanning the samples in the range of wavelengths from 200 to 800 nm, with sintered PTFE serving as a reference standard throughout the experiment. The specific area (S_{BET}) and pore size distribution were determined by nitrogen physisorption isotherms of the as-prepared samples recorded at 77 K with ASAP 2020 Plus (Micromeritics Instrument Corporation, USA) instrument. The NP samples were degassed for 10 h at 120°C under ultra-high vacuum prior to the tests. The BET equation and BJH method were used to determine the surface area and the pore size distributions, respectively.

The *p*H drift method was used to determine the as-synthesised NPs' point of zero charge (pH_{PZC}) [74]. As a baseline electrolyte, eight 200-mL 0.1M KNO_3 solutions were prepared.

Background electrolyte KNO_3 was used to maintain the solution's ionic strength at a constant level. The initial *p*H of the electrolyte solution was kept between 4 and 12 by employing 0.1M HCl or 0.1M NaOH. Solutions with varying *p*H values were shaken for 24 h with 0.15 g TiO_2 NPs. The final *p*H values (pH_{final}) were then determined. The pH_{pzc} of TiO_2 NPs was measured at the *p*H where $pH_{initial}$ - pH_{final}.

Photocatalytic experiment

The photocatalytic activities of the as-prepared TiO_2NCsand commercial TiO_2 (Degussa, P-25) were investigated by degrading MB dye irradiated with a high-pressure mercury UV lamp (Model: MBFU 125W E27, OSRAM). The photodegradation tests were carried out by setting the UV lamp over a 200-mL beaker at a temperature of 25°C. Prior to exposure to UV radiation, 0.1 g TiO_2 NPs were added to a 100 mL solution of MB with a concentration of 10 mg/L, and rapidly agitated for 30 min in dark to achieve adsorption equilibrium. All the photocatalytic experiment was carried at *p*H 7. After 30 min of stirring in the dark, the solution of MB (10 mg/L) at *p*H 7 was illuminated with a 0.1 g photocatalyst in the dark. After a specified time interval of light irradiation, 4 mL of the suspensions were taken as a sample and centrifuged. A UV-vis spectrophotometer (UV-1650, SHIMADZU, Japan) was used to measure the concentration of MB in the supernatant. Experiments without UV light irradiation using TiO_2 photocatalysts were also conducted as a control. In addition, experiments were also carried out without the photocatalyst but with UV exposure. Experiments with commercial TiO_2 (Degussa, P-25) were also carried out as a photocatalytic benchmark for comparability purposes. In other cases, four successive cycles of photodegradation of MB with a catalyst of 1.0 g L^{-1} at a dye concentration of 10 mg L^{-1} were carried out in order to explore the stability of the photocatalysts. Following a thorough cleaning with distilled water, a fresh solution of MB was added to the catalyst before each cycle, and this technique was repeated for each cycle in the experiment.

COD was measured using a photometer (MD 600, Lovibond, Germany) to make sure that the photodegradation process had been completed. In a typical experimental approach, Lovibond COD tube test containing 2 mL sample was cooked at 150°C. The COD of the sample was then evaluated after it had been digested and cooled to room temperature. Blank experiment was also performed in order to calibrate the photometer.

Results and Discussion

Characterization of NPs

In order to determine the crystallinity and size of the as-synthesized nanoparticles, XRD examination

was carried out. XRD patterns of TiO_2 produced by hydrothermal process at temperature of 150°C are shown in Fig. 1. The major diffraction lines shown in Fig. 1 at 2θ = 25.32°, 37.86°, 48.06°, 53.98°, 55.09°, and 62.76° which were attributed to the (101), (004), (200), (105), (211), and (204) planes of anatase phase TiO_2, respectively (JCPDS card No. 21-1272)[49,75]. It is also worth noting that the XRD pattern shows no other diffraction peaks matching to other phases of TiO_2 (such as rutile and brookite) or other crystalline impurities. Furthermore, applying the Debye–Scherrer equation (Eq. 1), the average crystallite size (D) of the produced TO_2 was estimated using the strongest (101) plane diffraction peak:

$$D = k\lambda / \beta\cos\theta \qquad \ldots(1)$$

where the symbols carry the usual meaning. The value of k is around 0.9, which is known as the "shape factor". In accordance with this equation, the calculated average crystallite sizes of the hydrothermally treated TiO_2 at 150, 200, and 220°C were found to be 8.3, 12.7, and 13.6 nm, respectively.

Additionally, Raman spectroscopy, which is a complementary approach to XRD, is an effective method for the identification of phases, the estimation of particle sizes, and the analysis of the microstructure of nanomaterials. The Raman spectroscopy can be used to distinguish between the anatase and rutile phases of titanium dioxide. Thus, anatase TiO_2 is projected to have six Raman-active modes (A1g + 2B1g + 3Eg) based on factor group analysis. The Raman spectrum of anatase single crystal published by Arsov *et al.*[76], reveals that the six permissible modes are located at 144 cm^{-1} (Eg), 197 cm^{-1} (Eg), 399 cm^{-1} (B1g), 516 cm^{-1} (A1g), 516 cm^{-1} (B1g), and 639 cm^{-1} (Eg). Figure 2 displays the Raman spectra of the TiO_2 nanoparticles prepared by hydrothermal method treated at different temperature. All the spectra are characteristic of the anatase TiO_2 phase, which confirmed the phase obtained by XRD. All of the spectra exhibit the distinctive peaks of anatase TiO_2. As shown in Fig. 2, the Raman peaks detected at 146, 199, 400, 519, and 640 cm^{-1} can be ascribed to the Eg, Eg, B1g, A1g + B1g, and Eg modes of anatase TiO_2, respectively. These findings are consistent with those published in the literature[77]. From Fig. 2, it is obvious that the Raman peak of the Eg mode of TiO_2 shifts to a higher wavenumber (146 cm^{-1}) when compared to the bulk value of Eg mode (144 cm^{-1}). This Raman shift can be attributed to the phonon confinement[78,79].

The crystallinity and morphology of the hydrothermally produced samples were further examined using transmission electron microscopy (TEM). Figure 3 shows the TEM and HRTEM images of the TiO_2 nanocomposite. The as-prepared TiO_2 sample Fig. 3(a) was found to be porous in nature, with an average particle size of roughly 8.2 nm, which was in good agreement with the average crystallite values measured by XRD. Furthermore, as indicated in the inset of Fig. 3(b), the observed lattice fringe corresponds to distances of 0.356 nm, which were consistent with the distances of the (101) lattice plane. The selected area diffraction pattern (SAED) shown in the inset of Fig. 3(b) also confirmed the crystalline anatase phase, in agreement with the X-ray diffraction data.

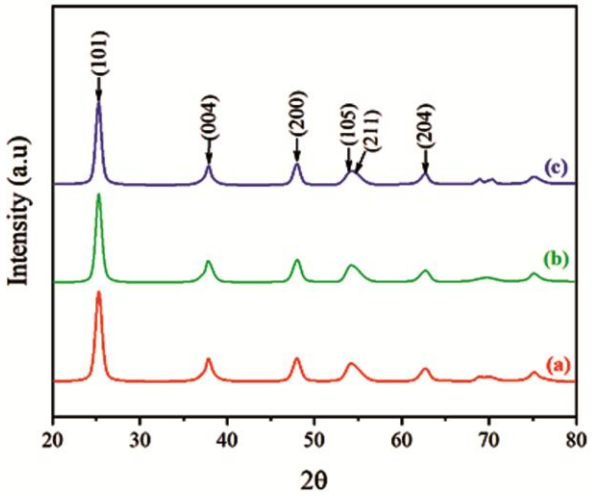

Fig. 1 — XRD spectra of vTiO_2prepared by hydrothermal method treated at (a) 150ºC; (b) 200ºC and (c) 220ºC.

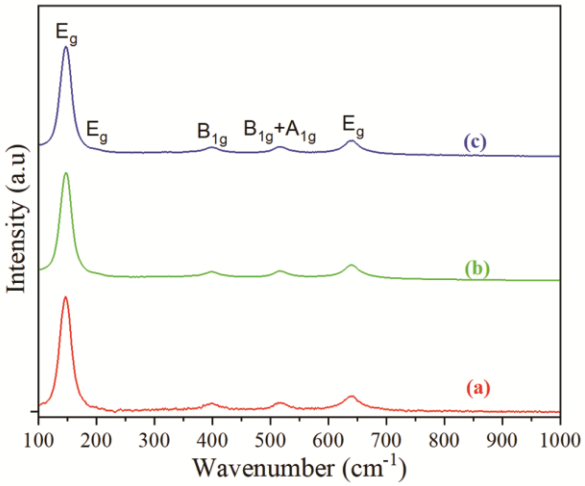

Fig. 2 — Raman spectra of TiO_2prepared by hydrothermal method treated at (a) 150ºC; (b) 200ºC and (c) 220ºC.

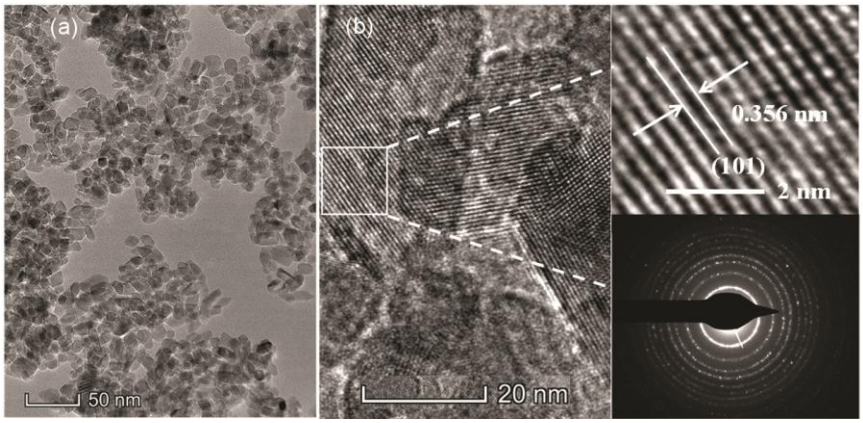

Fig. 3 — (a) TEM and (b) HRTEM images of hydrothermally prepared TiO_2 NCs. Inset shows the SEAD pattern and enlarged view of HRTEM.

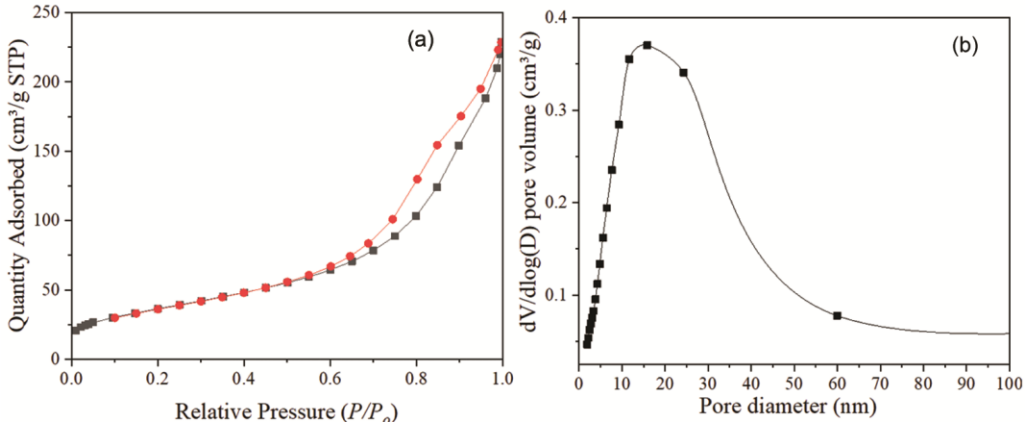

Fig. 4 — (a) N_2 adsorption–desorption isotherm and (b) pore size distribution of as-synthesized TiO_2 nanoparticles hydrothermal treated at 150ºC.

The mesoporosity and textural characteristics of TiO_2 catalysts were investigated using N_2 adsorption–desorption measurements at liquid N_2 temperatures. The isotherm of nitrogen adsorption and the pore size distribution of TiO_2 photocatalyst prepared by hydrothermal treatment at 150°C are depicted in Fig. 4. As per the IUPAC classification, the synthesized TiO_2 isotherm revealed in Figure 4(a) exhibited a type IV sorption behaviour with a type H2 hysteresis, which is typical of mesoporous materials. The H2-hysteresis demonstrated the existence of non-uniform pores in solids made of particles connected by approximately cylinder-shaped channels or produced by aggregates of spherical particles or agglomerates of spherical shell particles[80]. All remaining TiO_2 samples treated at a variety of temperatures (not shown) demonstrated the same type isotherms indicative of mesoporous materials. The distributions of TiO_2 nanoparticles' pore size estimated by the BJH method were quite wide which ranged from 2 to 40 nm, with a mean pore size of 10.10 ± 0.05 nm Fig. 4(b). Textural parameters of mesoporous TiO_2 produced at different growth temperatures and the reference TiO_2P-25 are shown in Table 1. The TiO_2 grown at 150°C hydrothermal temperatures have a specific area of 133.45 m^2/g, a mean pore size of 10.12 nm (inside the mesopore region) and a total pore volume of 0.34 cm^3/g. As can be seen, the hydrothermal temperature had no significant effect on the pore diameter or the overall volume of the pores. Thus, TiO_2 photocatalysts produced at 220°C exhibited only a small reduction in BET surface area, i.e. 115.7 m^2/g compared to 133.45 m^2/g for TiO_2 photocatalysts synthesized at 150°C. As a result, based on N_2 adsorption–desorption and XRD measurements, the as-synthesized photocatalysts may be regarded to be nanocrystalline mesoporous materials.

Table 1 — Crystallite size and textural properties of TiO_2 prepared by hydrothermal technique treated at different temperature.

Samples	Hydrothermal temperature, °C	Crystallite Size, nm	BET Surface area, m^2/g	Mean pore diameter, nm	Total pore volume, cm^3/g
TiO_2	150	8.3	133.45	10.12 ± 0.5	0.34 ± 0.02
TiO_2	200	12.7	132.8 ± 2	10.87 ± 0.5	0.26 ± 0.02
TiO_2	220	13.6	115.7 ± 2	11.47 ± 0.5	0.33 ± 0.02
P25	-	-	47 ± 1	11.5 ± 0.5	0.13 ± 0.02

Semiconductors' optical properties like band gaps play a pivotal role in defining their photocatalytic activity for decomposition of organic dye. UV-Vis DRS shown in Fig. 5 was used to evaluate the optical characteristics of the as-synthesized NPs. The absorption edges of pure TiO_2 were exhibited in Fig. 5 at a wavelength of approximately 388 nm. The as-synthesized nanoparticles' energy band gap (*Eg*) was determined using the equation:

$$\alpha(h\nu) = A(h\nu - E_g)^n$$

where the symbols carry their usual meaning[81]. The power factor n is dictated by the type of optical transition that occurs in a semiconductor. The power number (n) has a value of 1/2 for permitted direct transitions and 2 for permitted indirect transitions. The value of direct band gap (n = 1/2) is calculated by extrapolating a straight line to the x axis, $(\alpha E)^2 = 0$ whereas the indirect band gap (n = 2) is calculated by extrapolating a straight line to $(\alpha E)^{1/2} = 0$[82]. The remission function, *F(R)*, can often be used in place of the absorption coefficient, (α). Kubelka-Munk theory says this can be represented in terms of reflectance (R) as

$$\alpha/s = F(R) = (1-R)^2/(2R),$$

where *s* signifies the scattering coefficients[83]. Thus, the energy band gap of direct and indirect transition can be determined from the tangent of the plot $(F(R)\ h\nu)^2$ versus. $h\nu$ and $(F(R)\ h\nu)^{1/2}$ versus. hν, respectively. Based on the assumption that TiO_2 is an indirect band gap semiconductor, the optical band gaps of the as-prepared samples were calculated from Figure 4(b) by extrapolating the linear sections of the $(F(R)\ h\nu)^{1/2}$ against $h\nu$ curves Fig. 6. According to the literature, anatase TiO_2 has a band gap energy of 3.20-3.56 eV [84]. The predicted *Eg* for TiO_2 was found to be 3.20 eV regardless of hydrothermal temperature, which was in good accord with the values reported elsewhere [19,85,86].

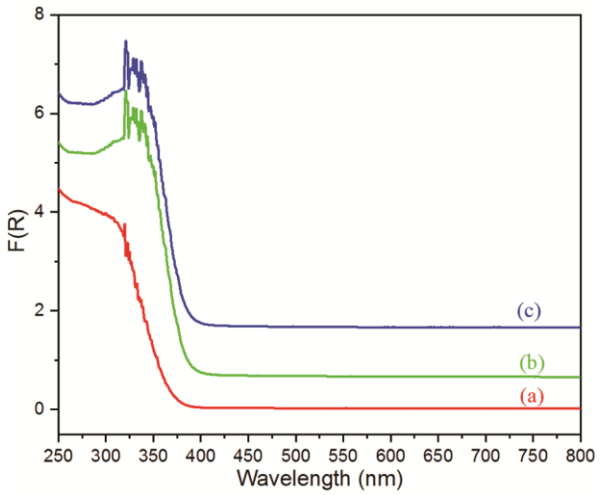

Fig. 5 — UV-visible diffuse reflectance spectra of TiO_2 synthesized at hydrothermal temperature (a) 150ºC; (b) 200ºC and (c) 220ºC.

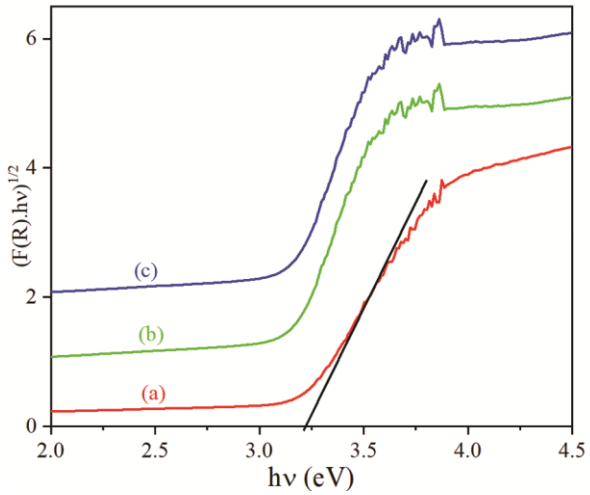

Fig. 6 — $[F(R)\ h\nu]^{1/2}$ versus $h\nu$ plot and (B)$[F(R)\ h\nu]^2$ versus $h\nu$ plot of TiO_2 nanoparticles synthesized at hydrothermal temperature (a) 150ºC; (b) 200ºC and (c) 220ºC.

Photocatalytic activity investigation of TiO_2 NCs

The photocatalytic activity of TiO_2 NCs' was examined by degrading MB dye illuminated with UV light. TiO_2 and commercial P25 were used as controls

for the photocatalytic degradation of MB. Furthermore, the photocatalytic activity of MB was evaluated as a blank experiment utilizing only UV light illumination and without use of a photocatalyst in order to validate the degrading efficacy of TiO_2 NCs. As a blank experiment, the photocatalytic degradation of MB under only UV light irradiation and without the use of photocatalyst was also tested. MB adsorption onto TiO_2 NCs without illumination was also examined as a blank test. The result of preliminary study presented in Fig. 7(a-b) revealed that when MB dye solution containing dispersed TiO_2 NCs was irradiated with UV light, the color of the solution gradually faded, indicating the decomposition of the MB dye's chromophoric structure. The efficiency of photocatalytic activity of TiO_2 photocatalysts synthesized at different hydrothermal temperature are demonstrated in Fig. 8(a-b). The degradation efficiency was determined by dividing the concentration of MB dye (C) at any point of time by the original concentration (C_O) of MB. From Fig. 8(a), it is observed that the TiO_2prepared at hydrothermal temperature 150°C showed higher degradation efficiency compared to TiO_2 prepared at other temperature and commercial P-25. After around 20 min of photocatalysis, the photocatalytic efficiency of TiO_2 produced at 150, 200 and 220ºC and P-25 for the decomposition of MB was approximately 94, 91, 90 and 78%, respectively. In summary, mesoporous TiO_2 nanoparticles generated at hydrothermal temperatures of 150°C had the fastest MB decomposition rate, confirming the approach presented in this study. A pseudo-first order kinetic rate rule is widely accepted to explain the kinetic of photodegradation of organics. The logarithm form of first law for photodegradation of organics is expressed as:

$$\ln(C/C_0) = -kt,$$

where k denotes the rate constant. The slope of the plot $\ln(C/C_0)$ versus time will give the value of reaction rate constant, k. TiO_2 NC degrading efficiency was proven by plotting $\ln(C/C_0)$ against

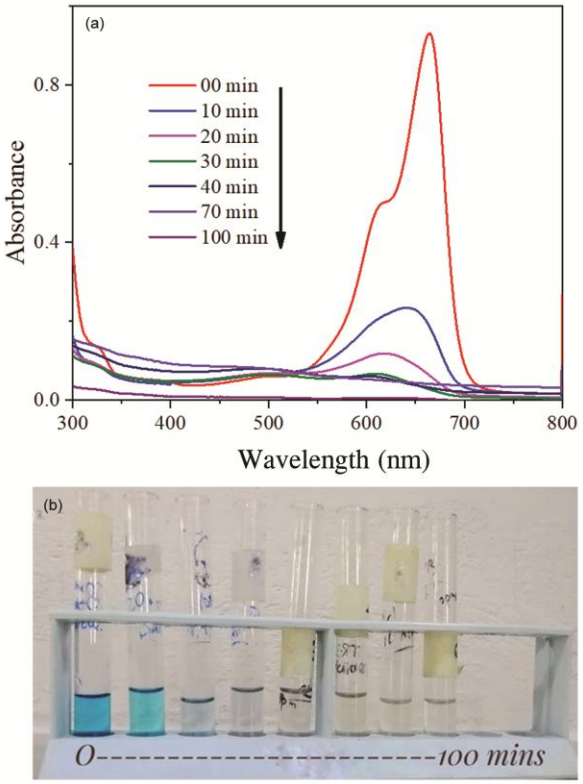

Fig 7 — Time-dependent changes in (a) absorbance and (b) colour of MB solution in the presence of TiO_2 nanomaterials under UV light.

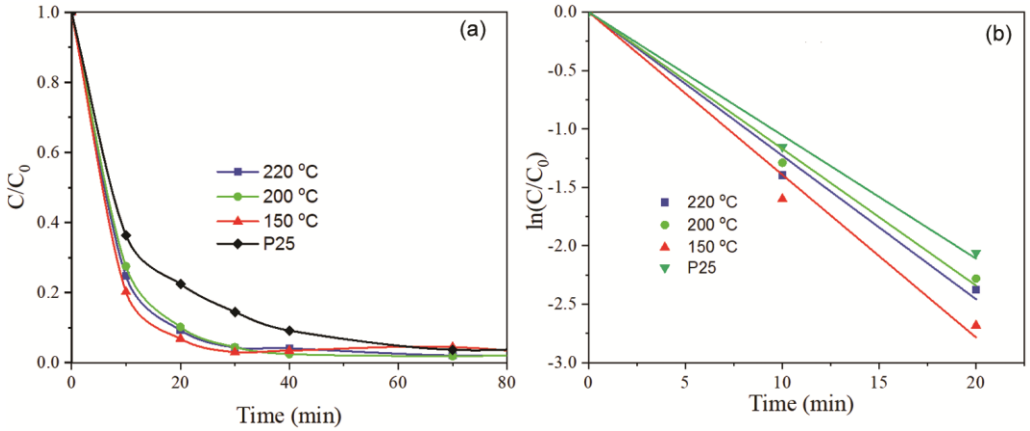

Fig. 8 — (a) Photocatalytic degradation efficiencies and (b) $\ln(C/C_0)$ versus irradiation time plot for the decomposition of MB with TiO_2 photocatalyst prepared at different hydrothermal temperature.

time, *t*, as illustrated in Fig. 8(b). The experimental values of ln(C/C_0) were plotted against time, *t* (shown in Fig 8(a)) in order to evidence the higher degradation efficiency of TiO_2 NCs. From Fig. 8(b), it is obvious that the TiO_2 NCs produced at hydrothermal temperatures of 150°C exhibited higher degradation efficiency with degradation rate constant 0.139 min^{-1}, the results achieved was approximately 1.54 times higher than that obtained with the commercial P25.

It is important to note at this point that the photocatalytic activity of photocatalysts is dependent on a variety of parameters, including their optical absorption characteristics, texturing parameters like specific areas and average pore size[87]. As a result, the increased specific area of hydrothermally generated TiO_2 nanoparticles might be used to explain the improved photocatalytic capabilities of the nanoparticles. A large surface area accounts for a substantial density of localized states, which would provide advantageous charge separation in the form of trapping sites for photo-generated charge carriers[88,89]. The change in photocatalytic activity might also be caused by the coupling of materials with differing band gaps, which favors the electron-hole charge separation, as has been shown for a variety of metal oxide heterojunctions in the literature[19,37]. However, XRD data shows that the only crystalline phase present in the samples is anatase TiO_2, making this explanation less plausible than the others.

The degradation mechanism is explained in Fig. 9 and Scheme 1. Electrons in VB of TiO_2 are stimulated to the CB when they are irradiated with ultraviolet light (UV). They migrate to the surface of the photocatalyst and participate in a redox reaction with the organics that are already present on the catalyst's surface. In the conduction band, photo-generated electrons react with dissolved oxygen, creating superoxide radical anions, $O_2^{\bullet-}$, which on protonation producehydroperoxy radicals $HO_2^{\bullet}$ and eventually $OH^{\bullet}$radicals. The photogenerated holes, on the other hand, participate in the oxidation reaction with the surface hydroxyl group or physisorbed water molecules, resulting in the formation of the hydroxyl radical, $OH^{\bullet}$. The $OH^{\bullet}$radicals are a strong oxidizing agent well-known to decompose organic substrates as MB dye to the degradation products H_2O and CO_2.

The *p*H of the solution is an important parameter in the photocatalytic reactions that take place on particulate surfaces because it controls the surface charge characteristics of the photocatalyst. Fig. 10(a)

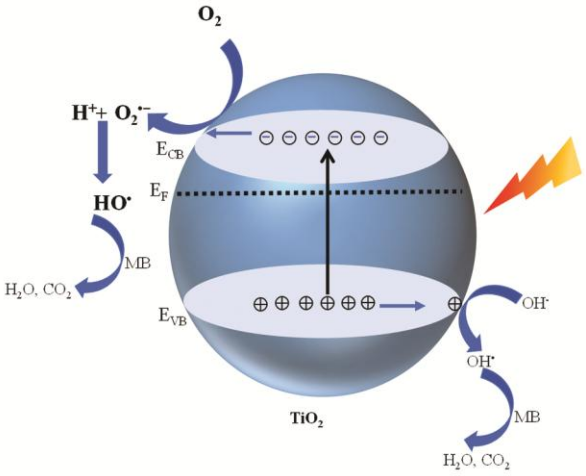

Fig. 9 — Graphical representation of photocatalytic decomposition of MB by TiO_2 nanoparticles.

$$TiO_2 + h\nu \rightarrow TiO_2.e_{cb}^- + TiO_2\ h_{vb}^+$$

$$TiO_2.e_{cb}^- + O_2 \rightarrow O_2^{\bullet-}$$

$$O_2^{\bullet-} + H^+ \rightarrow HO^{\bullet}$$

$$O_2^{\bullet-} + H_2O \rightarrow HO_2^{\bullet} + OH^-$$

$$HO_2^{\bullet} + H_2O \rightarrow HO^{\bullet} + H_2O_2$$

$$H_2O_2 \rightarrow 2HO^{\bullet}$$

$$TiO_2\ h_{vb}^+ + OH^- \rightarrow HO^{\bullet}$$

$$MB + HO^{\bullet} \rightarrow \text{Degradation products}$$

Scheme 1 — Proposed reaction mechanism for photocatalytic decomposition of MB under UV light irradiation

shows the effect of *p*H on the degradation efficiency of TiO_2 photocatalyst for the degradation of MB. According to the Fig. 10(a), basic media was favorable for the photocatalytic degradation of MB. The degradation efficiencies observed at *p*H values of 3.0, 7.1 and 10 were 35%, 92% and 99.97%, respectively. The enhanced photocatalytic activity at higher *p*H can be explained with the help of pH_{PZC}. The pH_{PZC} of TiO_2 was determined to be 7 ± 0.2 (Fig. 10b). At *p*H > pH_{PZC} the TiO_2 surface becomes negative charge and below pH_{PZC} the surface becomes positively charged. Therefore, the cationic dye MB was easily adsorbed on the negatively charged TiO_2 NPs by an electrostatic attraction which is prerequisite for heterogeneous photocatalysis.

The catalysts' stability and reusability were tested by exposing them to the same conditions four times

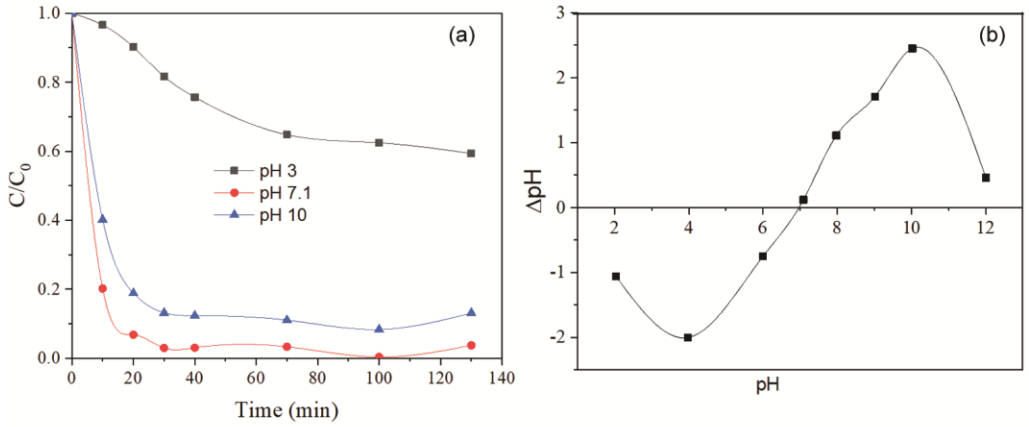

Fig 10 — (a) Effect of *p*H on degradation efficiency of TiO_2 and (b) pH_{PZC} of TiO_2.

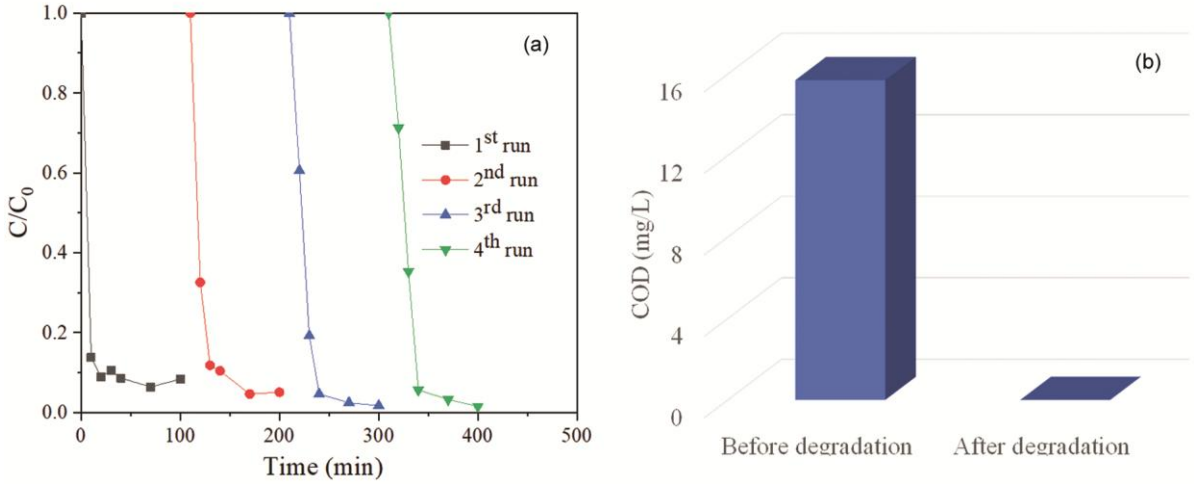

Fig. 11— (a) Recyclability of synthesize TiO_2 photocatalyst and (b) COD values of MB before and after photocatalytic degradation with TiO_2.

in a row. Fig. 11(a) depicts the recurrent photo-degradation of MB that occurs over the course of four consecutive cycles. The result showed that after 30 minutes of reaction time in each cycle, the photocatalytic efficiencies for the four cycling uses were 97, 93, 92 and 92%, respectively. The fact that there was no substantial change in the catalytic efficiency for the degradation of MB demonstrated the stability and reusability of the catalysts used in the experiment. In addition, completely mineralization of organic dye MB to CO_2 and H_2O by photocatalytic degradation with the as-prepared photocatalyst was confirmed by COD analysis. The results are presented in Fig. 11(b). According to the Fig. 11(b), the COD value of MB solution before UV irradiation was about 15.7 mg/L whereas no COD value of the same sample was observed after photocatalytic degradation which evidenced the complete mineralization of organic dyes.

Conclusion

In this study, the hydrothermal approach has been successfully used to prepare nanostructured TiO_2 photocatalysts. In accordance with the XRD results, the TiO_2 nanoparticles are found to be in the normal anatase phase, and the average crystallite size of TiO_2 produced at 150°C is determined to be around 8.3. The produced nanoparticle is mesoporous, having a specific surface area of 133.45 m^2/g. Photocatalytic activity of the produced TiO_2 nanoparticles for the degradation of MB under UV light irradiation is found to be outstanding. It is found that the *p*H of the solution had a direct impact on the photocatalytic process, with a basic *p*H being more favorable for the breakdown of MB. The photocatalytic activity of the TiO_2 photocatalyst for the degradation of methylene blue dye is found to be higher than that of the reference commercial TiO_2 P25. The degradation is

favourable at basic media and the prepared TiO_2 is stable even after four consecutive cycles. Finally, the COD analysis confirm the complete mineralization of dye in H_2O and CO_2. This approach of semiconducting nanocatalysts with strong photocatalytic activity should find practical application in the future.

Acknowledgement

Authors would like to thank Shahjalal University of Science and Technology (SUST)Research Center for financial support (Grant no. AS/2018/3/35) to conduct this work.

References

1 Lellis B, Fávaro-Polonio C Z, Pamphile J A & Polonio J C, *Biotechnol Res Innov*, 3 (2019) 275.
2 Garg V K, Kumar R & Gupta R, *Dye Pigment*, 62 (2004) 1.
3 Hagan E & Poulin J, *Herit Sci*, 33(2021) 9.
4 Ogugbue C J & Sawidis T, *Biotechnol Res Int*, 2011 (2011) 1.
5 Chandanshive V, Kadam S, Rane N, Jeon B H, Jadhav J & Govindwar S, *Chemosphere*, 252 (2020) 126513.
6 Adane T, Adugna A T & Alemayehu E, *J Chem*, 2021 (2021) 1.
7 Şen S & Demirer G N, *Water Res*, 37 (2003) 1868.
8 dos Santos A B, Cervantes F J & van Lier J B, *Bioresour Technol*, 98 (2007) 2369.
9 Ben M H, Houas I, Montassar F, Ghedira K, Barillier D, Mosrati R & Chekir-Ghedira L, *Environ Sci Pollut Res*, 19 (2012) 2634.
10 dos Santos A B, Cervantes F J & van Lier J B, *Bioresour Technol*, 98 (2007) 2369.
11 Hassan M M & Carr C M, *Chemosphere*, 209 (2018) 201.
12 Przystas W, Zablocka-Godlewska E & Grabinska-Sota E, *Water Air Soil Pollut*, 223 (2012) 1581.
13 Berradi M, Hsissou R, Khudhair M, Assouag M, Cherkaoui O, El Bachiri A & El Harfi A, *Heliyon*, 5 (2019) e02711.
14 Khatri J, Nidheesh P V, Anantha S T S & Kumar S M, *Chem Eng J*, 348 (2018) 67.
15 Carneiro P A, Umbuzeiro G A, Oliveira D P & Zanoni M V B, *J Hazard Mater*, 174 (2010) 694.
16 Ferraz E R A, Umbuzeiro G A, de-Almeida G, Caloto-Oliveira A, Chequer F M D, Zanoni M V B, Dorta D J & Oliveira D P, *Environ Toxicol*, 26 (2011) 489.
17 Mukhlish M Z B, Islam M A, Rahman M A, Hossain S, Islam M A & Uddin M T, *Desalin Water Treat*, 230 (2021) 169.
18 Uddin M T, Mukhlish M Z Bin & Patwary M R H, *Desalin Water Treat*, 212 (2021) 311.
19 Uddin M T, Nicolas Y, Olivier C, Toupance T, Müller M M, Kleebe H J, Rachut K, Ziegler J, Klein A & JaegermannW, *J Phys Chem C*, 117 (2013) 22098.
20 Uddin M T, Nicolas Y, Olivier C, Toupance T, Servant L, Müller M M, Kleebe H J, Ziegler J & Jaegermann W, *Inorg Chem*, 51 (2012) 7764.
21 Ibhadon A O & Fitzpatrick P, *Catalysts*, 3 (2013) 189.
22 Ahmed S, Rasul M G, Martens W N, Brown R & Hashib M A, *Water Air Soil Pollut*, 215 (2011) 3.
23 Ahmed S N & Haider W, *Nanotechnology*, 29 (2018) 34.
24 Linsebigler A L, Lu G & Yates J T, *Chem Rev*, 95 (1995) 735.
25 Mamaghani A H, Haghighat F & Lee C S, *Appl Catal B Environ*, 203 (2017) 247.
26 Li Y W & Ma W L, *Chemosphere*, 280 (2021) 130667.
27 Fujishima A & Honda K, *Nature*, 238 (1972) 37.
28 Lee C G, Javed H, Zhang D, Kim J H, Westerhoff P, Li Q & Alvarez P J J, *Environ Sci Technol*, 52 (2018) 4285.
29 Chen D, Cheng Y, Zhou N, Chen P, Wang Y, Li K, Huo S, Cheng P, Peng P, Zhang R, Wang L, Liu H, Liu Y & Ruan R, *J Clean Prod*, 268 (2020) 121725.
30 Sun Q, Li K, Wu S, Han B, Sui L & Dong L, *New J Chem*, 44 (2020) 1942.
31 Bin Mukhlish M Z, Najnin F, Rahman M M & Uddin M J, *J Sci Res*, 5 (2013) 301.
32 Chen W T, Chan A, Jovic V, Sun-Waterhouse D, Murai K I, Idriss H & Waterhouse G I N, *Top Catal*, 58 (2015) 85.
33 Ohtani B, *Catalysts*, 3 (2013) 942.
34 Guayaquil-Sosa J F, Serrano-Rosales B, Valadés-Pelayo P J & de Lasa H, *Appl Catal B Environ*, 211 (2017) 337.
35 Hu Y, Song X, Jiang S & Wei C, *Chem Eng J*, 274 (2015) 102.
36 Uddin M T, Nicolas Y, Olivier C, Servant L, Toupance T, Li S, Klein A & Jaegermann W, *Phys Chem Chem Phys*, 17 (2015) 5090.
37 Uddin M T, Babot O, Thomas L, Olivier C, Redaelli M, D'Arienzo M, Morazzoni F, Jaegermann W, Rockstroh N, Junge H &Toupance T, *J Phys Chem C*, 119 (2015) 7006.
38 Allen N S, Mahdjoub N, Vishnyakov V, Kelly P J & Kriek R J, *Polym Degrad Stab*, 150 (2018) 131.
39 Zhu T & Gao S P, *J Phys Chem C*, 118 (2014) 11385.
40 Hanaor D A H & Sorrell C C, *J Mater Sci*, 46 (2011) 855.
41 Li J G & Ishigaki T, *Acta Mater*, 52 (2004) 5143.
42 Di Paola A, Bellardita M & Palmisano L, *Catalysts*, 3 (2013) 36.
43 Luttrell T, Halpegamage S, Tao J, Kramer A, Sutter E & Batzill M, *Sci Rep*, 4 (2014) 4043.
44 Augustynski J, *Electrochim Acta*, 38 (1993) 43.
45 Sclafani A & Herrmann J M, *J Phys Chem*, 100 (1996) 13655.
46 Li Z, Cong S & Xu Y, *ACS Catal*, 4 (2014) 3273.
47 Liu L, Zhao H, Andino J M & Li Y, *ACS Catal*, 2 (2012) 817.
48 Nateq M H & Ceccato R, *Adv Mater Sci Eng*, 2019 (2019) 1.
49 Uddin M T, Nicolas Y, Olivier C, Jaegermann W, Rockstroh N, Junge H & Toupance T, *Phys Chem Chem Phys*, 19 (2017) 19279.
50 Sun H, Wang C, Pang S, Li X, Tao Y, Tang H & Liu M, *J Non Cryst Solids*, 354 (2008) 1440.
51 Zhou M, Roualdès S, Zhao J, Autès V & Ayral A, *Thin Solid Films*, 589 (2015) 770.
52 Le M T, Nguyen H L, Vu A T, Nguyen V C & Wu J C S, *J Chinese Chem Soc*, 66 (2019) 1713.
53 Dobrovolskiy A, Goncharov A, Kostin E & Frolova E, *Probl At Sci Technol*, 94 (2014) 145.
54 Chen Y, Huang B, Huang M & Cai B, *J Taiwan Inst Chem Eng*, 42 (2011) 837.
55 Santhi K, Navaneethan M, Harish S, Ponnusamy S & Muthamizhchelvan C, *Appl Surf Sci*, 500 (2020) 144058.
56 Anjugam V S A, Pugazhenthiran N, Mangalaraja R V, Sathishkumar P, Viswanathan B & Anandan S, *ACS Omega*, 3 (2018) 9834.
57 Wu X, Yin S, Dong Q, Guo C, Li H, Kimura T & Sato T, *Appl Catal B Environ*, 142 (2013) 450.

58 Guo J, Zhu S, Chen Z, Li Y, Yu Z, Liu Q, Li J, Feng C & Zhang D, *Ultrason Sonochem* 18 (2011) 1082.
59 Mao L, Liu J, Zhu S, Zhang D, Chen Z & Chen C, *Ultrason Sonochem*, 21 (2014) 527.
60 Prabhudesai V S, Meshram A A, Vinu R & Sontakke S M, *Chem Eng J Adv*, 5 (2021) 100084.
61 Nagaveni K, Sivalingam G, Hegde M S & Madras G, *Environ Sci Technol*, 38 (2004) 1600.
62 Nagaveni K, Sivalingam G, Hegde M S & Madras G, *Appl Catal B Environ*, 48 (2004) 83.
63 Nassar M Y, Ali E I & Zakaria E S, *RSC Adv*, 7 (2017) 8034.
64 Cui X, Wang J, Zhang X, Wang Q, Song M & Chai J, *Langmuir*, 35 (2019) 9255.
65 Li X, Zheng W, He G, Zhao R & Liu D, *ACS Sustain Chem Eng*, 2 (2014) 288.
66 Lee M S, Lee G D, Ju C S & Hong S S, *Sol Energy Mater Sol Cells*, 88 (2005) 389.
67 Zubieta C E, Soltero - Martínez J F A, Luengo C V & Schulz P C, *Powder Technol*, 212 (2011) 410.
68 Kubiak A, Bielan Z, Bartkowiak A, Gabała E, Piasecki A, Zalas M, Zielińska-Jurek A, Janczarek M & Siwińska-Ciesielczyk K& Jesionowski T, *Catalysts*, 10 (2020) 586.
69 Li L, Zhang X, Zhang W, Wang L, Chen X & Gao Y, *Colloids Surfaces A Physicochem Eng Asp*, 457 (2014) 134.
70 Cano-Casanova L, Amorós-Pérez A, Ouzzine M, Lillo-Ródenas M A & Román-Martínez M C, *Appl Catal B Environ*, 220 (2018) 645.
71 Wang G, *J Mol Catal A Chem*, 274 (2007) 185.
72 Yin H, Wada Y, Kitamura T, Kambe S, Murasawa S, Mori H, Sakata T & Yanagida S, *J Mater Chem*, 11 (2001) 1694.
73 Jesty T & Reddy M L P, *Int J Nanotechnol*, 8 (2011) 841.
74 Babić B M, Milonjić S K, Polovina M J & Kaludierović B V, *Carbon N Y*, 37 (1999) 477.
75 Sreethawong T, Yamada Y, Kobayashi T & Yoshikawa S, *J Mol Catal A Chem*, 241 (2005) 23.
76 Arsov L D, Kormann C & Plieth W, *J Raman Spectrosc*, 22 (1991) 573.
77 Li W S, Shen Z X, Li H Y, Shen D Z & Fan X W, *J Raman Spectrosc*, 32 (2001) 862.
78 Arora A K, Rajalakshmi M, Ravindran T R & Sivasubramanian V, *J Raman Spectrosc*, 38 (2007) 604.
79 Balaji S, Djaoued Y & Robichaud J, *J Raman Spectrosc*, 37 (2006) 1416.
80 Leofanti G, Padovan M, Tozzola G & Venturelli B, *Catal Today*, 41 (1998) 207.
81 Davis E A & Mott N F, *Philos Mag*, 22 (1970) 903.
82 Sanchez E & Lopez T, *Mater Lett*, 25 (1995) 271.
83 Murphy A B, *Sol Energy Mater Sol Cells*, 91 (2007) 1326.
84 Nakaruk A,Ragazzon D & Sorrell C C, *Thin Solid Films*, 518 (2010) 3735.
85 Lee D Y, Kim J T, Park J H, Kim Y H, Lee I K, Lee M H & Kim B Y, *Curr Appl Phys*, 13 (2013) 1301.
86 Zhang W, Song N, Guan L X, Li F & Yao M M, *J Exp Nanosci*, 11 (2016) 185.
87 Bhattacharjee A, Ahmaruzzaman M & Sinha T, *Spectrochim JeActa - Part A Mol Biomol Spectrosc*, 136 (2015) 751.
88 Barzykin A V & Tachiya M, *J Phys Chem B*, 106 (2002) 4356.
89 Qian R, Zong H, Schneider J, Zhou G, Zhao T, Li Y, Yang J, Bahnemann D W & Pan J H, *Catal Today*, 335 (2019) 78.